Construction and Building Materials 428 (2024) 136376

Contents lists available at ScienceDirect

Construction and Building Materials

journal homepage: www.elsevier.com/locate/conbuildmat

Automating the determination of low-temperature fracture resistance curves of normal and rubberized asphalt concrete in single-edge notched beam tests using convolutional neural networks

Sepehr Ghafari [a,*], Fereidoon Moghadas Nejad [b], Akbar Sheikh-Akbari [a], Hadi Kazemi [a]

[a] School of Built Environment, Engineering and Computing, Leeds Beckett University, United Kingdom
[b] Department of Civil & Environmental Engineering, Amirkabir University of Technology (Tehran polytechnic), Iran

ARTICLE INFO

Keywords:
Fracture resistance curves
Bituminous mixtures
Rubberized asphalt concrete
Convolutional neural networks
Growing crack
Crack length
Fracture energy

ABSTRACT

As materials undergo large-scale yielding or exhibit large sizes of fracture process zone in the crack tip region, multi-parameter fracture concepts should be employed to describe the complex crack-tip stress-strain fields. Fracture resistance curves (R-curves) are an established tool in characterizing the entire fracture process of such materials. However, for complex materials such as bituminous mixtures, the development of these curves is subject to experimental and computational intricacies. In this research, a framework is developed to automate the construction of R-curves for normal and rubberized asphalt concrete (AC) mixtures. AC mixtures are produced using PG58–22 and PG58–28 binders. Limestone and siliceous aggregates are used, and three binder contents are considered for the mixtures. Single-edge notched beam (SE(B)) fracture testing is conducted on AC beams with two different notch patterns. A convolutional neural network (CNN) model is developed and trained over 1260 test images with varying temperatures, notch geometries, and setups. The CNN model was used to detect the growing crack on the beam surface and each crack-detected image was sent to an image processing framework to measure the crack length. Crack extension increments were calculated and synchronized with test time and magnitude of load, load-line displacement, and cumulative fracture energy, and the R-curve could be constructed. A training accuracy of 0.91 was obtained for the model and a loss of below 0.10 as a result of a hyperparameter tuning indicating reliable classifications by the CNN architecture. The R-curves showed desirable agreement for control mixtures at temperatures of 0 °C and −15 °C. As the mixtures are rubberized, the R-curves showed favorable agreement in the crack blunting phase, transition zone, as well as the unstable propagation phase at −20 °C. Cohesive energy magnitudes were compared for the two methods with a Pearson coefficient of 0.81 while fracture rate and fracture energy magnitudes showed favorably close magnitudes with coefficients of 0.89 and 0.98 respectively.

1. Introduction

Non-linear, inelastic materials undergo significant amounts of plastic deformation in the crack tip region when subject to loading [1]. In general, the size and extent of this plastic zone is influenced by the yield strength and toughness of the material [1,2]. This region influences the strain and stress fields ahead of the crack tip and mechanisms such as micro-void coalescence and shear banding are intensified within this zone. In cases where the plastic zone is small compared to all other pertinent dimensions of the cracked body (i.e., crack size, uncracked ligament), a K-controlled zone ahead of the crack tip can be a valid assumption. However, more advanced fracture concepts must be instrumented to describe the complex crack tip stress-strain region for materials with large-scale plastic zones and no stress singularity e.g., the J-integral. In this fashion, fracture resistance curves (R-curves) can represent the variation in fracture resistance of the material with the extension of the crack. The resistance can be expressed in terms of an energy-based parameter, often J-integral, to account for the nonlinear responses and offer insights into the realistic fracture trend of such complex materials. While extensive body of research is available for fracture analysis of metals [3,4], fracture and crack growth characterization of bituminous mixtures using R-curves is still scarce due to

* Corresponding author.
E-mail addresses: s.ghafari@leedsbeckett.ac.uk (S. Ghafari), moghadas@aut.ac.ir (F.M. Nejad), a.sheikh-akbari@leedsbeckett.ac.uk (A. Sheikh-Akbari), h.kazemi@leedsbeckett.ac.uk (H. Kazemi).

https://doi.org/10.1016/j.conbuildmat.2024.136376
Received 20 December 2023; Received in revised form 24 February 2024; Accepted 22 April 2024
Available online 25 April 2024

experimental intricacies.

In 2015, Ghafari and Nejad [5,6] derived J-resistance curves for hot mix asphalt (HMA) mixtures and addressed the R-curve sensitivity to the varying factors in their research such as temperature and binder content. A rising R-curve was observed in their research for moderate to low temperatures and fracture instability (J_{inst}) magnitudes were determined following an approach employed for metals. In later research [7,8], Ghafari and Nejad applied the J-R curve concept to study the effect of crumb rubber incorporation in asphalt concrete mixtures using warm-mix technology. They extracted parameters such as the peak load and the corresponding crack length and critical J-integral magnitudes as well as the rate of change in J-integral by crack extension in the post-peak region. They concluded that a 20% crumb rubber addition could significantly contribute to enlarging the stable crack growth zone at low temperatures (-20 °C in their research) and reshaping the R-curve to a progressively rising state. Efforts have been made to investigate the effect of additives or binder replacements [9] on the R-curve of bituminous mixtures. Yang and Braham [10] constructed the resistance curves of asphalt concrete mixtures employing semi-circular bend (SC(B)) testing at medium to low temperatures and investigated the effect of temperature, polymer modification, binder grade, gradation, and loading rate on these curves. They presented the R-curves in terms of cumulative fracture energy versus crack extension and extracted three quantitative parameters: cohesive energy, fracture energy, and fracture rate from the curves. They found that polymer modification had significantly affected crack initiation despite the lower grade of the binder. It was also observed in this study that higher testing temperatures result in higher creep energy during the fracture process which is more associated with the propagation phase than the crack initiation. In another research, Yang and Braham [11] investigated the effect of binder ageing on R-curves of HMA. According to this research, long-term ageing could significantly reduce the cohesive energy, fracture rate, and total fracture energy of the mixtures. Furthermore, R-curves were developed for mixed-mode (I/II) loading conditions for hot mix asphalt mixtures [12,13]. A single-edge notched beam (SE(B)) setup was utilized and the experiments were conducted in a range of moderate to low temperatures. Continuous acquisition of high-quality digital images was carried out during each test and the crack extensions were obtained by a manual crack length measurement in each image. They observed that the crack blunting zone of the R-curve is significantly influenced as the mode II loading component is increased. Moreover, unstable crack propagation of the mixtures was substantially reduced as mode II loading contribution dominated the tensile loading mode.

Despite the advantages of R-curve analysis for bituminous mixtures, developing the fracture resistance curves for non-metal materials is known to be time-consuming, substantially complex, and having high experimental costs. Efforts have been made to develop compliance equations for asphalt concrete [14] to use a single-specimen technique using the unloading compliance method similar to metals for HMA as well. However, mixture-specific characteristics could potentially reduce the precision of the equations, therefore a massive dataset of mixtures would be required to develop reliable compliance equations. Furthermore, Liu and Yang [15] proposed an alternative method for crack length extension in R-curve analysis of asphalt concrete. They applied the digital image correlation (DIC) technique to capture the displacement field around the crack tip on an SC(B) test setup and construct the R-curve of the mixtures using the crack opening displacement matrix (CODM) on the specimen surface. The displacements in the CODM were used as crack extensions to construct the R-curve. Moreover, using DIC has gained wide-spread attention among researchers in the past two decades as a robust technique to study stain mapping of asphalt mixtures [16–19]. Asghar and Khattak used the DIC to investigate the fracture and fatigue properties of a novel hot mix asphalt (HMA). They used crumb rubber and polyvinyl alcohol fibers in developing the HMA. Leveraging DIC, they observed that the HMA composite developed by rubber fiber had a larger strain distribution which led to crack bridging and higher fracture resistance in this material [20–22].

To further facilitate the use of R-curves for crack propagation analysis of asphalt mixtures, authors developed a machine learning (ML) framework [23] to predict the fracture resistance curves of the mixtures using multi-gene genetic programming (MGGP). They used a wide range of variables such as binder grade, binder content, aggregate type, and temperature to develop a consistent dataset of mixtures and applied artificial neural networks (ANN). Even though a desirable agreement was observed between the predicted R-curve and the measured ones, however, a massive dataset is still required to rely on the ML model as a standalone framework for predicting R-curves.

As can be inferred, employing the R-curve concept can be significantly beneficial in characterizing the entire fracture process of bituminous materials subject to varying parameters in terms of mixture properties and environmental conditions. However, Determination of these curves for bituminous materials requires extensive experimental capacity and effort. The most reliable single-specimen method to develop R-curves includes capturing consecutive images during the test and manually calculating the crack extension increments which is excessively time-consuming and could be subject to human errors. Furthermore, manual (human) inspection of all the captured images is required in this method and images with the growing crack need to be screened and attributed to the corresponding magnitudes of load, load-line displacements (LLD), and finally fracture energy so the R-curve could be constructed. This research is aimed at leveraging an efficient convolutional neural network architecture to classify the images that contain the crack as the loading and crack growth continues. The cracked area is automatically cropped which will significantly reduce the noise occurring from the pores on the specimen surface. These images are automatically synchronized with the corresponding magnitudes of load and LLD. The crack length is calculated through the image processing module and the pairs of (cumulative fracture energy, crack extension) can be plotted in an entirely automated process. Therefore, this framework will significantly reduce experimental time and costs for developing R-curves for bituminous materials offsetting the need for manual (human inspection of every captured image).

Hot mix asphalt mixtures were produced using limestone and siliceous aggregates. Three binder contents were considered for the mixtures and PG58–22 and PG58–28 grade bitumen were used. Mixtures with 20% crumb rubber and 3% warm-mix additive were developed in addition to control mixtures. Asphalt concrete beams were fabricated from slabs and SE(B) testing was carried out on them at temperature levels of 0 °C, −15 °C, and −20 °C. High-quality digital images were captured continuously during each test. The images were fed into a CNN model trained over 1260 images from SE(B) tests and the images with growing crack were classified and sent to the crack length measurement module. Crack lengths and extensions were calculated by processing the images and the results were synchronized with the time of test, magnitude of load, load-line displacement, and the corresponding cumulative fracture energy. Cumulative fracture energy was then plotted versus crack extensions for each experiment and the R-curve could be constructed.

2. Objective

The impetus for this research was to harness a deep learning framework to offset the experimental and manual processing of data required to construct a fracture resistance curve for asphalt concrete. In line with this, convolutional neural networks are leveraged to carry out an automated image classification into cracked and uncracked images and export the cracked area to the image processing stage. This will replace the time-consuming manual inspection and screening of the acquired images and also significantly reduces the excessive noise detected due to beam surface pores as the images are auto cropped. Each image containing crack is then synchronized with the corresponding value of load (P) and load-line displacement (LLD) and the cumulative

fracture energy can be calculated and plotted versus the crack length to construct the R-curve. A visual illustration of the proposed framework is presented in Fig. 1 and the objectives can be concisely summarized as the following:

- Developing a convolutional neural network model for real-time image classification to detect images with the growing crack during each test.
- Automated cropping of the cracked area by the bounding box segmented by the CNN model.
- Synchronizing the cropped image with the corresponding magnitudes of load and load-line displacement.
- Calculating crack extension increments from the cropped images exported to the image processing module.
- Calculating cumulative fracture energy using the load and load-line displacements and plotting the R-curve in terms of cumulative fracture energy vs. crack extension.

3. Materials and methods

3.1. Materials and specimen preparation

Asphalt concrete mixtures with siliceous and limestone aggregates were prepared in this research. Limestone aggregates were grey in color and crushed while siliceous aggregates were uncrushed with a variety of surface colors. The physical properties of the aggregates are presented in Table 1. PG 58–22 and PG 58–28 were used for preparing mixtures and the base binders with physical and rheological properties as in Table 2. The nominal maximum aggregate size for both mixtures was 19 mm as plotted in Table 3. The optimum binder content of the mixtures was determined using the Marshall method. This value was obtained to be in the range 4.5%±0.2% for different mixtures in this research. Therefore, the optimum binder content for all the mixtures were considered equal to 4.5%. Furthermore, a ±0.5% jump in the binder content was used (bringing the binder content to 4% and 5%) in developing the test specimens as contents below and above the optimum content are reported to have tangible effects on the fracture trend of the mixtures [24,25]. Specimens with lower binder contents are reported to undergo brittle fracture earlier than those with higher contents and the specimens with higher binder contents are reported to have larger transition zones (from crack blunting to unstable propagation) and a notable energy dissipation in the unstable propagation zone [7,12]. Therefore, varying crack propagation characteristics in the mixtures attempted to investigate the performance of the automated framework on varying trends of the fracture process in mixtures. Therefore, Mixtures were developed using 4%, 4.5%, and 5% binder content as an influential parameter on instability and brittleness of the mixtures [26] at low temperatures and hence inducing various crack orientations. All the

Table 1
Physical properties of the limestone and siliceous aggregates.

Property	Standard	Limestone aggregate	Siliceous aggregate
LA Abrasion loss	AASHTO T96–02	20	19
Fractured in one face	ASTM D5821–13	>98	>87
Fracture in two faces	ASTM D5821–13	>98	93
Flakiness	BS 812–103.1	5	20
Coating of aggregate	AASHTO T184	98	95
Sodium Sulphate loss	AASHTO T104–99	1.8 (fines) 0.7 (coarse)	2.8 (fines) 0.4 (coarse)

Table 2
Physical and rheological properties of the binders.

Property	PG58-22	PG58-28	Test Method
Penetration at 25 °C, 0.1 mm	89	180	ASTM D5
Softening point (°C)	50.8	38	ASTM D36
Ductility (15 °C, cm)	>100	>100	ASTM D113
Flashing point (°C)	290	230	ASTM D92
Density	1.02	1.033	ASTM D70
Kinematic viscosity (Centistoke, 135 °C)	370	300	ASTM D2170
Kinematic viscosity (Centistoke, 160 °C)	130	135	ASTM D2170
DSR (G*/sin(δ), kPa)	1.29	1.99	ASTM D7175

Table 3
Limestone and siliceous aggregate gradation for AC mixtures.

Size (mm)	Passing (%)
25	100
19	100
12.5	95
4.75 (Sieve No. 4)	59
2.36	43
0.3	13
0.075 (Sieve No. 200)	6

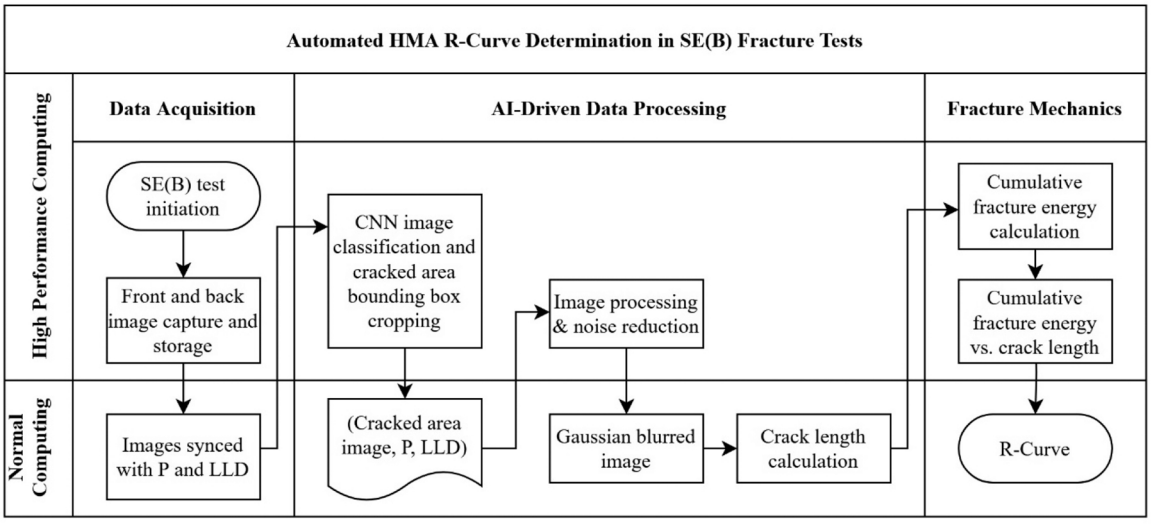

Fig. 1. Automated R-curve construction framework for asphalt concrete mixture.

mixtures were prepared unmodified (control mixtures) as well as modified by 20% crumb rubber by weight of the base binder.

Ground crumb rubber particles with a maximum size of 0.6 mm (#30) were mixed with the base bitumen using 3% warm-mix additive (Sasobit) prior to blending with the aggregate. The mixing was carried out in a high-shear mixer applying a rotational velocity of 6000 rpm at 160 °C for 15 minutes in the first stage. The temperature was then elevated to 180 °C and a steady state mixing continued for 30 minutes at a reduced velocity of 2000 rpm giving a homogenous rubberized binder [27–30]. The binder is then mixed with the heated aggregate and compacted in the slab mold at a temperature of 170 °C to a void ratio of 4%±1%.

The molds were cooled to room temperature for 7 hours and AC slabs were then extracted from the molds. Three AC beam specimens were fabricated from each slab having a height (B) of 40 mm, a width (W) of 80 mm, and a gross span length of 380 mm (net span length of S=320 mm). AC beam dimensions were selected based on ASTM E1820–20b instructions giving a notch length of 16 mm (S=4 W, W/B=2, a/W=0.2). Two different methods were employed to fabricate the mechanical notch in the AC beams. For the specimens with limestone aggregates, an 8 mm base was first cut through the height of the beam using the automated water-cooled saw having a blade thickness of 5 mm. The remaining 8 mm was then cut using a hand saw having a 1 mm thick blade. AC beams with limestone aggregate and the two-stage mechanical notch can be seen in Fig. 2. This two-stage notch fabrication could minimize excessive blunting and branching at the notch tip as the crack initiates [31,32]. For the specimens with siliceous aggregates, the entire 16 mm notch length was cut using an automated saw with a blade thickness of 2.5 mm. A handsaw with a blade thickness of 1 mm could not be used for these samples due to the significant resistance of the siliceous aggregate against the blade. AC beams with siliceous aggregate having a range of grain colors can be seen in Fig. 2.

3.2. SE(B) test with image acquisition and classification

Single-edge bend tests are carried out in this research to construct the fracture resistance curves for asphalt concrete mixture at low temperatures. The test setup and configurations including fixture dimensions, AC beam dimensions, etc. fundamentally comply with ASTM E399–20a [33] and ASTM E1820–20b [34] instructions. The experiments were conducted in a universal testing machine (UTM) capable of various modes of loading equipped with an environmental chamber capable of providing customized monotonous low temperatures. The AC beam samples were conditioned inside the environmental chamber at least 4 hours prior to being mounted on the beam support. Two high-resolution digital cameras were installed on the two sides of the fixture focusing on the center of the beam span to capture the propagating crack during the tests. Tests were run with and without infrared illumination. The illumination was provided using Infra-red light emitting diode (IR LED) bulb pads on the two sides of the fixture without disturbing uniform temperature distribution across the chamber.

A preload of 0.1 kN was applied to the beam on the mid-span to ensure consistent seating of the sample on the supports. The test was then initiated using a vertical loading rate of 5 mm/min for most of the conditions. The two digital cameras were triggered to capture continuous images of the specimen surface during the test. Each test continued up to the failure of the specimen or where the load magnitude reached a value of approximately 0.1 kN. A code was developed to extract and interpret EXIF data of the images as well as to read the feedback from the UTM actuator linear variable digital transformer. Object arrays consisting of images, capture time and date, magnitude of load, and load-line displacement were then generated by the code. Images with the corresponding values of load and load-line displacement at an interval of 1 s for each test were batched and introduced to the CNN model as a new dataset for each test to screen cracked samples from uncracked images. The values of the load and load-line displacement (LLD) were used to calculate the cumulative fracture energy [35–40] and the images containing a crack were then classified by the model and were input to the image processing module to calculate the length of the propagating crack. The results from the image processing module were then populated with the corresponding value of cumulative fracture energy as a two-element array representing a unique point in the R-curve plot.

3.3. Convolutional neural network (CNN)

3.3.1. CNN model architecture

The CNN model developed comprises multiple convolutional and pooling layers, with connected (dense) layers at the end for classification. The model is designed for binary image classification and the details and architecture are presented in Table 4 and Fig. 3 respectively.

3.3.2. Convolutional layer

In CNN, the convolutional layer plays the fundamental role in the sense that it learns the features from the captured image. The input

Table 4
Details of the CNN model structure and the image dataset.

Model and Dataset Properties	Values
Convolution3D	3
Maxpooling3D	3
Flatten	1
Dense	1
Image dataset	1260
Cracked images	844
Uncracked images	416
Raw image resolution	2592×1944
Image size	1.5–3.0 MB

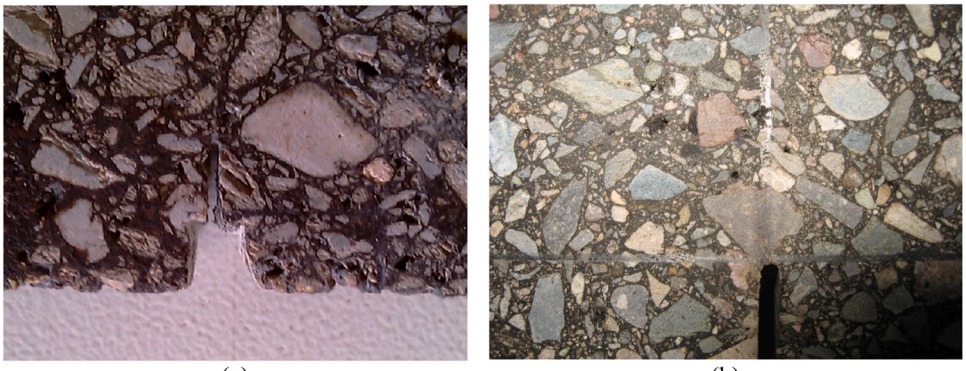

(a) (b)

Fig. 2. Notch patterns for specimens: a) with limestone aggregate b) siliceous aggregate.

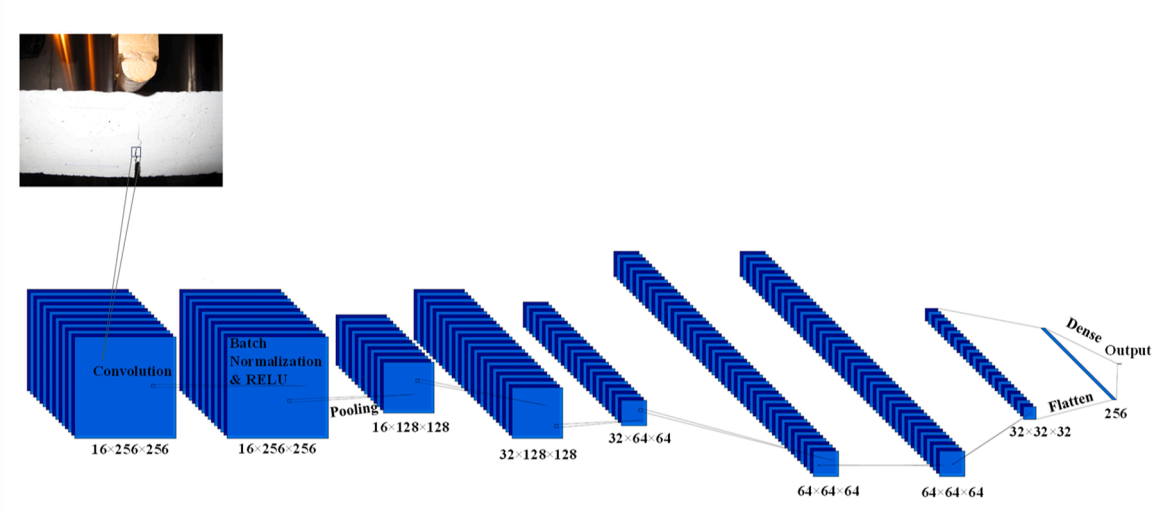

Fig. 3. Graphical illustration of the CNN model architecture.

image size introduced to the model is considered to have 256 pixels in height, and 256 pixels in width with RGB channels. The input shape is only required in the top convolutional layer. In the sequential model constructed, 16 kernels were defined for each convolutional layer. Therefore, 16 filters are applied to the input image for detecting different patterns. The convolved image is the result of a convolution process in which each pixel in the input image is matrix-multiplied by the kernel which is a small-size matrix (3×3 pixels here). The convolution operation can be expressed as in eq. 1:

$$O = \left| \frac{\sum_{i=1}^{n} \left[\sum_{j=1}^{n} c_{ij} d_{ij} \right]}{\sum_{i=1}^{n} c_{ij} \neq 0} \right| \quad (1)$$

Where:

O: Output pixel value

n: Kernel dimension (i.e. 3×3 here)

c_{ij}: Coefficient element in the kernel matrix

d_{ij}: Image matrix element

As a result, this process obtains local patterns, and a feature map can be generated. In the initial convolutional layers, the introduction of the filters leads to the detection of low-level features e.g., edges, and corners. By stacking multiple convolutional layers, higher-level filters combine, and more complex patterns can be identified.

3.3.3. Activation function

An activation function is assigned to each neuron in a neural network which is a mathematical function. This mathematical function introduces non-linearity to the network i.e., intricate relationships can be modelled between the inputs and outputs. These functions contribute significantly to the efficiency of the model as they perform neuron-wise to determine the outputs. The Rectified Linear Unit (ReLU) activation function is used for the convolutional layers while the Sigmoid is used for the output layer.

ReLU is one of the most commonly used activation functions in convolutional neural networks due to its efficiency. The mathematical expression for ReLU can be found in eq. 2:

$$f(x) = ReLU(x) = \max(0, x) \quad (2)$$

Where:

x: Input to the function.

The function returns 1 for any positive input. In the case of using gradient-based learning scenarios for training the ANNs, as the gradients may turn into vanishingly small values, they can prevent the weights from changing values and consequently, the neural network may prematurely stop training [41,42]. This issue can be alleviated by using the simple but computationally efficient ReLU activation function. Furthermore, the entire efficiency and convergence of the model is also enhanced.

The Sigmoid activation function is used in the output layer which is a popular function used in binary classifications i.e. the neuron output classes are assigned probabilities. The mathematical expression of the Sigmoid activation function is presented in eq. 3:

$$f(x) = Sigmoid(x) = \frac{1}{1 + \exp(-x)} \quad (3)$$

Where:

x: Input to the function.

The Sigmoid activation function transforms the input into a value ranging from 0 to 1, which can be interpreted as the probability of the input belonging to a certain class. One advantage of the Sigmoid activation functions is that backpropagation can be conducted by them since they are differentiable with regard to the input. However, they can potentially halt the network from further learning as a vanishing gradient problem is likely to occur while using them [43].

3.3.4. Pooling

Pooling layers inserted between successive convolutional layers play a key role in reducing the spatial dimensions of the inputs. These layers down-sample the feature maps generated by each convolutional layer. Max pooling is used here as the most common type and strategy in deep convolutional networks. In this technique, the pooling operation is applied to different regions of the feature map and the maximum value from each local neighborhood of the input is extracted. Therefore, the spatial dimensions of the feature map are reduced, and a representative pixel value (maximum) is selected. This operation will reduce the computational complexity for the proceeding layers of the model while leading to improved processing efficiency [44]. A pooling window with a size of 2×2 is specified in this model.

3.3.5. Flatten layer

Flatten layers are typically used in deep CNN architectures before the dense layers. The main purpose of introducing flatten layers is to reshape the feature maps output from the convolutional layers since dense layers require 1-dimensional inputs. In other words, the feature maps resulting from convolutional layers, are transformed into 1-dimensional tensors

spatially before being input to the subsequent dense layers. The predictions are then made based on the flattened features.

3.3.6. Batch normalization

Cross-entropy loss is a commonly used loss function in classification problems in deep learning [44]. In this fashion, the binary cross-entropy loss function is used when implementing binary classification tasks, where it is intended to predict only one class. The function determines the dissimilarity or error between the predicted probability by the model and the true binary label for each sample. The binary cross-entropy function is presented in eq. 4:

$$Binary \quad Cross-Entropy \quad Loss = -\frac{1}{n}\sum_{i=1}^{n}[y_i \log[p(y_i)] + (1-y_i)\log[1-p(y_i)]] \tag{4}$$

Where:

y_i : The actual class

$p(y_i)$: The probability of 1

In the cracked beam detection problem two classes labeled 1 (cracked) and 0 (uncracked) beam images are defined. The binary cross-entropy function penalizes the model if the prediction is close to 0 in the case of a cracked beam image while the penalization is triggered again if the prediction is near 1 for an uncracked image. The loss is then calculated as the average of these penalizations over the batch of samples. As the model is trained across the dataset, the binary cross-entropy loss is to be minimized, hence, the accuracy of model predictions is improved.

3.3.7. Model training

The CNN model was trained on 1260 test images. The images included uncracked samples, loaded beam samples prior to the initiation of a visible crack, samples with the propagating crack as well as samples at test termination. Fig. 4 presents sample images used to train the model for uncracked conditions.

Varying illumination conditions were used for the tests. Most of the samples were tested under the UTM-provided lighting. Nevertheless, some of the samples were tested under infrared illumination. AC beam samples were developed from limestone and siliceous aggregates. A two-stage notch was fabricated for limestone samples while a simple notch (16 mm) was cut in the siliceous samples (Fig. 2). 85% of the samples were beams painted in white while 15% were unpainted samples. Fig. 5 shows sample cracked AC beams used for training the model.

3.3.8. Hyperparameter tuning

Hyperparameter tuning is considered a crucial step in the development of machine learning models, including Convolutional Neural Networks. It entails systematic exploration of different hyperparameter values to optimize the performance of the model on a given task. Hyperparameters, are settings that are set before training commences, therefore, are not learned during training and could potentially play a significant role in model performance and behavior. The hyperparameters in an image classification CNN include learning rate, optimizer type, kernel size, batch size, dropout rate, etc. Several methods are available for hyperparameter tuning, including grid search, random search, Bayesian optimization, etc. A grid search approach was employed for hyperparameter tuning in this research, to explore possible enhancements to the accuracy of the CNN image classification model.

A grid of hyperparameters: learning rates, optimizers, and kernel sizes was defined for this research forming the search space as the following:

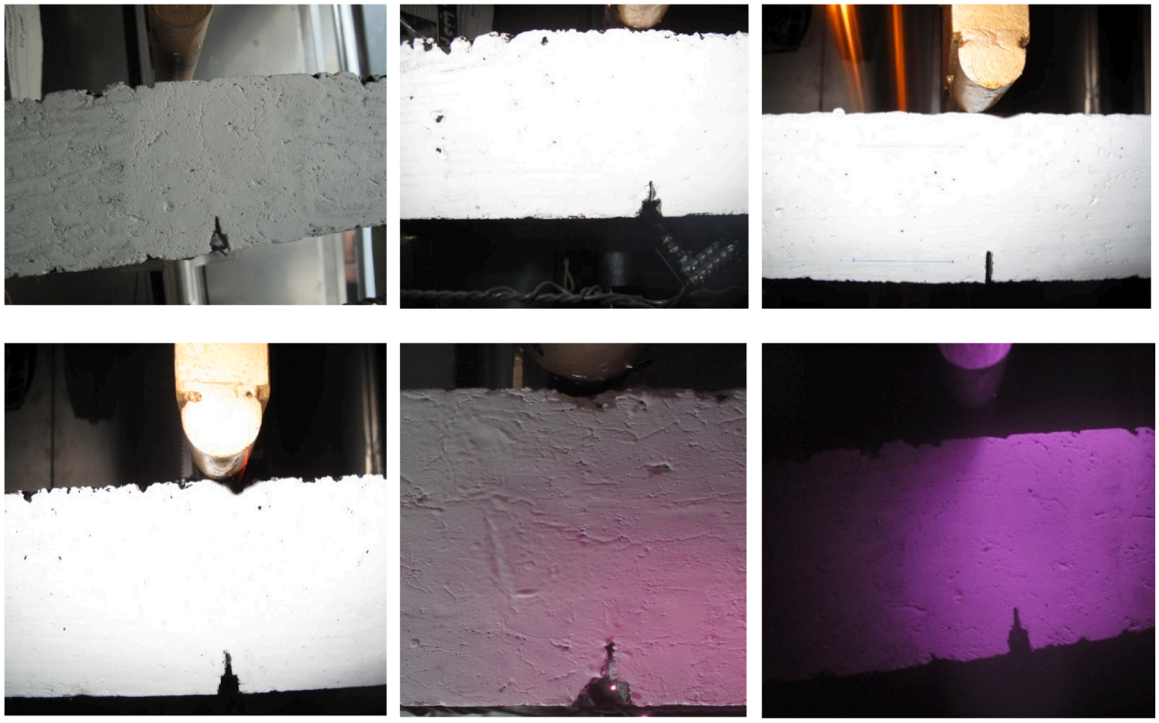

Fig. 4. Sample uncracked annotations.

Fig. 5. Samples used for cracked beam annotations.

Learning rates: [0.001, 0.01, 0.1]
Optimizers: rmsprop, adam
Kernel sizes: [(3, 3), (5, 5), (7, 7)]

Where adam (adaptive moment estimation) and rmsprop (adaptive moment estimation) are two widely used optimization algorithms commonly used in training neural networks, including CNNs: rmsprop is an adaptive learning rate optimization algorithm that addresses some limitations of AdaGrad [45]. It maintains a moving average of the squared gradients for each parameter, adjusting the learning rate based on the average of the recent gradients. This allows rmsprop to dynamically adapt the learning rate for each parameter, improving convergence and stability during training. Adam combines the benefits of two other optimization techniques: AdaGrad and rmsprop. It maintains adaptive learning rates for each parameter by computing individual adaptive learning rates for different parameters. Adam also incorporates momentum, which helps accelerate the optimization process by accumulating gradients from past iterations [44,46].

The dataset is split into training, validation, and possibly test subsets and cross-validation is carried out to assess model performance while mitigating overfitting and data leakage issues. The model is trained and evaluated using various hyperparameter combinations and the configuration yielding the best performance on the validation set is selected. The process was carried out utilizing GridSearchCV in scikit-learn library.

4. Results and discussion

4.1. Convergence

During the training process, the convergence and efficiency of the model is governed by multiple parameters such as the validation loss, validation accuracy, and number of epochs. In a convolutional neural network architecture, the convergence of the model typically means attaining a steady state during the training process where the model learns and updates its weights and biases through optimization algorithms. An optimal number of epochs of 150 was selected for the model. Parameter updating is conducted during each epoch as the model iterates across the entire dataset.

4.2. Validation accuracy

A validation process is carried out during the training process with a fraction of 15% of the training dataset. The validation accuracy reveals the ability of the model to make correct classifications from the validation subset. The model has not previously been exposed to the data selected for this subset during the training process. A high validation accuracy indicates a desirable training of the model in which the patterns are efficiently learned by the model and robust predictions are made for unseen (validation) without overfitting. However, low or declining values of validation accuracy typically indicate overfitting or a poor determination of the patterns by the model to predict the correct class from the unseen data. Here, a validation accuracy of above 0.97 was obtained after 150 epochs.

4.3. Validation loss

Validation loss can serve as another controlling metric for the overfitting of the model. The validation loss expresses the difference between the correct classification (true labels) and the prediction of the model quantitatively. A growing (increasing) validation loss could potentially indicate overfitting. Whereas a decreasing validation loss is typically indicative of the robustness of training and the ability of the model to learn patterns from the dataset and predict the correct label from the unseen validation set.

4.4. Training loss

The discrepancy (error) between the predictions of the model and the correct classifications (true labels) is revealed by the training loss. As previously addressed, minimizing the loss is the goal of the model and lower values of training loss can be associated with a desirable fitting of the training data for each epoch. The minimization is carried out by refining the weights and biases in the model and iterating over. Descending training loss is a desirable trend in the training process (remaining below 0.15 for the last 30 epochs here), however, this cannot be selected as the sole parameter to judge the effectiveness and performance of the model.

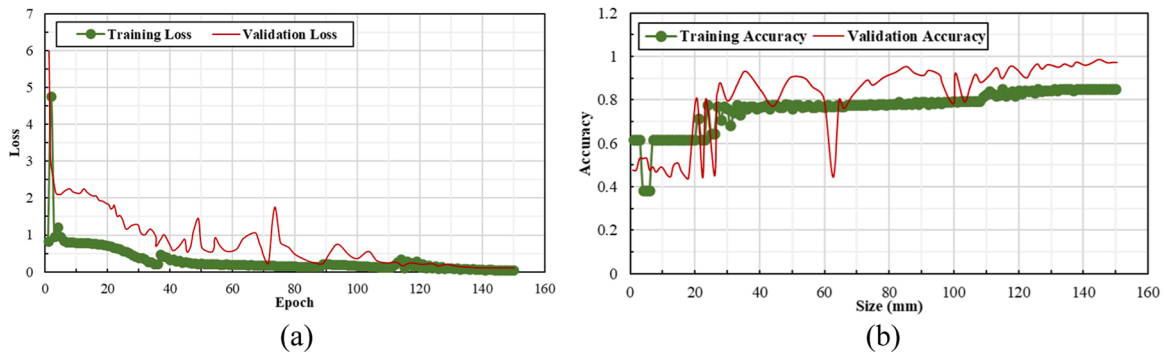

Fig. 6. Accuracy and loss of the CNN during validation and training: a) Training and validation loss, b) Training and validation accuracy.

4.5. Training accuracy

Training accuracy is a quantitative indication of the fraction of correct classifications by the model in the training dataset. This accuracy parameter represents the percentage of the correct predictions (classifications) across the training dataset during each epoch. Iteratively and as the training process proceeds and the model updates its weights, the training accuracy is expected to increase. Otherwise, the desirable performance might not be attained. The training accuracy can be used in conjunction with validation accuracy to give a definitive judgement of the efficiency of the model since the validation accuracy derives the metric over unseen data. A training accuracy of above 0.84 was obtained in this research after 150 epochs. Fig. 6 presents accuracy and loss values of the CNN during model validation and training procedures.

4.6. Hyperparameter tuning results and enhancements

The best-performing model was evaluated using a separate test dataset that was not used during the hyperparameter tuning process. This ensures an unbiased evaluation of the performance on unseen data. Hyperparameter configurations and the evaluation metrics are presented in Table 5. The mean_test_score in this table refers to the average accuracy of the model evaluated on the validation set across all splits of the cross-validation process. In the tuning process, the dataset is divided into multiple splits. The model is trained on a combination of these splits and evaluated on the remaining ones. This process is repeated multiple times, with each split being used as the validation set exactly once. The mean_test_score is then calculated as the average accuracy (serving as a performance metric) across all splits. Moreover, the std_test_score measures the intensity of the metric variation across these subsets and provides an indication of the consistency or stability of the performance of the model across different subsets of the data. Low values std_test_score indicate that the performance of the model is relatively consistent across different subsets, suggesting that the selected hyperparameters generalize well to unseen data. The mean_test_precision is a measure of the accuracy of the positive predictions made by the model. It quantifies the ratio of true positive predictions to the total number of positive predictions made by the model. In this model (cracked image classification), precision represents the proportion of correctly predicted cracked regions (true positives) among all regions predicted as cracked by the model (true positives + false positives). The mean_test_f1_score and std_test_f1_score represent the mean and standard deviation of F1 scores for the precisions, respectively [47].

Values of 0.01 for the learning rate, (3, 3) for the kernel size and adam optimizer were selected as the best-performing hyperparameters for the CNN model. The model is subsequently trained over the main dataset (1260 SE(B) test images) and the enhanced values of validation and loss can be seen in Fig. 7. It can be seen that the training accuracy of the CNN model is improved to approximately 0.91 as a result of hyperparameter tuning.

The training accuracy of 0.91 indicates that the model correctly classifies approximately 91% of the images in the training dataset. This level of accuracy suggests that the model has learned meaningful patterns and features from the training data, enabling it to make reliable predictions. A low training loss below 0.10 further reinforces the reliability of the model's predictions. The loss metric quantifies the discrepancy between the predicted and actual labels, with lower values indicating better alignment between predicted and true values. A loss below 0.10 suggests that the model has effectively minimized errors during training and is capable of making precise predictions/

Table 5
Hyperparameter combinations and model performance metrics.

Learning rate	Optimizer	Kernel size	test_accuracy	std_test_accuracy	mean_test_precision	std_test_precision	mean_test_f1_score	std_test_f1_score
0.001	adam	(3, 3)	0.87	0.012	0.89	0.013	0.86	0.011
0.001	adam	(5, 5)	0.89	0.011	0.88	0.012	0.88	0.01
0.001	adam	(7, 7)	0.86	0.014	0.88	0.01	0.86	0.012
0.001	rmsprop	(3, 3)	0.89	0.013	0.84	0.015	0.89	0.014
0.001	rmsprop	(5, 5)	0.87	0.011	0.86	0.012	0.87	0.011
0.001	rmsprop	(7, 7)	0.88	0.013	0.88	0.011	0.88	0.013
0.01	adam	(3, 3)	0.91	0.011	0.96	0.011	0.90	0.01
0.01	adam	(5, 5)	0.88	0.012	0.89	0.01	0.87	0.012
0.01	adam	(7, 7)	0.86	0.015	0.86	0.013	0.86	0.015
0.01	rmsprop	(3, 3)	0.87	0.013	0.86	0.014	0.87	0.012
0.01	rmsprop	(5, 5)	0.88	0.011	0.87	0.012	0.88	0.011
0.01	rmsprop	(7, 7)	0.87	0.012	0.88	0.013	0.87	0.012
0.1	adam	(3, 3)	0.88	0.014	0.87	0.013	0.88	0.014
0.1	adam	(5, 5)	0.86	0.013	0.86	0.014	0.86	0.013
0.1	adam	(7, 7)	0.85	0.014	0.89	0.013	0.85	0.014
0.1	rmsprop	(3, 3)	0.87	0.012	0.88	0.011	0.87	0.012
0.1	rmsprop	(5, 5)	0.88	0.013	0.87	0.012	0.88	0.013
0.1	rmsprop	(7, 7)	0.86	0.015	0.86	0.014	0.86	0.015

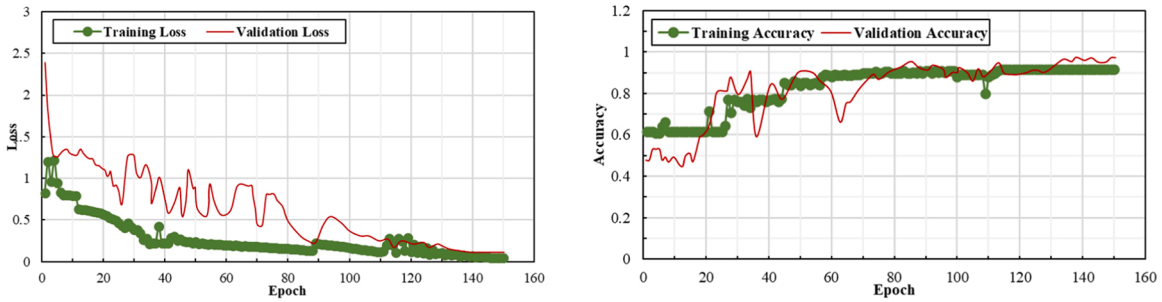

Fig. 7. Accuracy and loss of the CNN after hyperparameter tuning: a) Training and validation loss, b) Training and validation accuracy.

classifications. The precision of the model's classification refers to its ability to correctly identify positive cases (e.g., images containing crack) while minimizing false positives (incorrectly identifying non-cracked images as cracked). With a training accuracy of 0.91 and a low training loss, the model demonstrates a high level of precision in distinguishing between different classes of images. This precision is crucial in as the classified images are cropped (based on the bounding box around the cracked area proposed by the model) and exported to the image processing module.

4.7. Image classification and crack length detection

The performance of the model can be visualized over a range of SE(B) test images. Fig. 8 presents the CNN model's classification performance over sample test data with probabilities ranging from 0.84 to 0.97. The images used in this dataset are selected from loaded but uncracked samples, tests with IR illuminations, end-of test failed beams, as well as beams with propagating cracks. Since the model is trained over a wide range of images in SE(B) test setup, robust detection of the cracks can be seen in the test images. Additionally, and since the model was trained on raw test images, it is capable of seamless detection of the propagating crack over a wide range of images with varying configurations. Whereas the test fixture and beam surface voids could have been detected as cracks in case the model was trained solely on the cracked zone. The cropped crack image was then used for crack edge detection and length calculations.

Gaussian blur is applied to the cropped image in the first stage to minimize noise interferences. This is particularly useful in reduction of the occurring noise from the pores and aggregate/binder surface porosities in painted and unpainted specimens leading to improved edge detections and length measurements. The varying test conditions (painted/unpainted beams, and IR/UTM illuminations) potentially induces varying intensity levels in the images. Additionally, during each SE(B) test, load increments and further crack propagation induce varying intensity levels around the crack tip. Therefore, the gradient-based approach [48,49] allows for capturing intensity changes regardless of their levels. In terms of identifying continuous crack contours (Fig. 9), application of hysteretic thresholding aids in alleviating false detection of weak edges and hence strong edges are reliably differentiated.

As the loading continues in the SE(B) test, the crack tip extends. The growing crack exhibits varying intensity levels around the crack tip. Therefore, for the growing crack, this approach can significantly enhance continuous crack contour detection and ensure capturing the entire length of the crack. Fig. 10 shows the detected crack length increments during each test versus the values measured manually. It can be seen that the values agree very desirably with each other.

4.8. R-curve comparisons

Fracture resistance curves are constructed for all the mixtures using manual data pre-processing followed by calculations and the automated framework. Fig. 10 presents the R-curves for AC mixtures with limestone and siliceous aggregates at T=0 °C and T=-15 °C having PG58–22 binder. In terms of the low-temperature fracture performance of the mixtures, it can be noted that the R-curves for limestone mixtures stand higher than those for the mixtures with siliceous aggregate mixtures. This effect of aggregate on the R-curves is due to the lower bond ability and weaker bonds in the aggregate-binder interface in the mixture matrix for siliceous aggregate [5,10]. The lower R-curves for the siliceous aggregates can be noted by comparing Fig. 11 (c) with Fig. 11 (a) and (d) with Fig. 11 (b). For each mixture, the fracture resistance curve developed by the automated method is potted against the R-curve constructed using manual crack length measurements. It can be seen from the aforementioned temperature range that the machine-derived curve is in overall desirable proximity with the manually constructed R-curve which indicates the reliability of the proposed method. For each test at moderate to low temperatures (prior to T=-15 °C), the energy generated by load application is dissipated in blunting the notch tip before initiation of a mode I crack at the notch tip. This includes the process of coalescence of micro-scale voids in the notch tip region and the formation of cohesive surfaces leading to fracture or crack initiation. Looking at Fig. 11 (a) and (c), it can be seen that the R-curve is in a vertically rising state which corresponds to the energy dissipated for crack tip blunting. This phase is addressed as the crack blunting phase [1]. The point where the curve is detached from the y-axis is where the initial increment of crack extension is captured, and hence can be introduced as the cohesive energy [10,11]. Scrutinizing the crack blunting zone and the cohesive energy it can be seen that there exists a close agreement between the manually constructed R-curve and the AI-driven curve, whereas, for the low temperature range (Fig. 11 (b) and (d)), the two curves are exhibiting notable proximity in this phase.

As the R-curve deviates from the y-axis, the transition zone starts which includes a stable crack growth proceeded by an unstable propagation. It can be seen that the two methods are in close agreement in this zone while a degree of inconsistency can be seen in Fig. 11 (d) for a temperature of −15 °C which will be discussed together with the curves for siliceous aggregate and the −20 °C results.

Fig. 12 presents R-curves for mixtures produced using PG58–28 binder. It can be seen for this range of temperature that the resistance curves developed through the automated method are in desirable proximity to the manually derived R-curves. For the medium to low-temperature range (Fig. 12 (a) and 12 (c)), the crack blunting phase appears to be substantially similar in both methods and the same desirable agreement can be seen for T=-15 °C as well. All the mixtures exhibit a rising R-curve with a distinct cohesive energy followed by a stable crack growth zone before the unstable crack propagation phase. For each test, the loading continued up to a point of 0.1 kN or breakage of the specimen (total failure of the AC beam). Therefore, the y-axis value for the last point on the resistance curve corresponds to the total fracture energy of the mixtures. Comparing Fig. 11 (b) and (d) with Fig. 12 (b) and 12(d), it can be concluded that the mixtures produced by PG58–28 binder are exhibiting higher cohesive energy and fracture energy magnitudes at lower temperature ranges (-15 °C). This is due to the lower softening point in the PG58–28 binder (Table 2) which causes

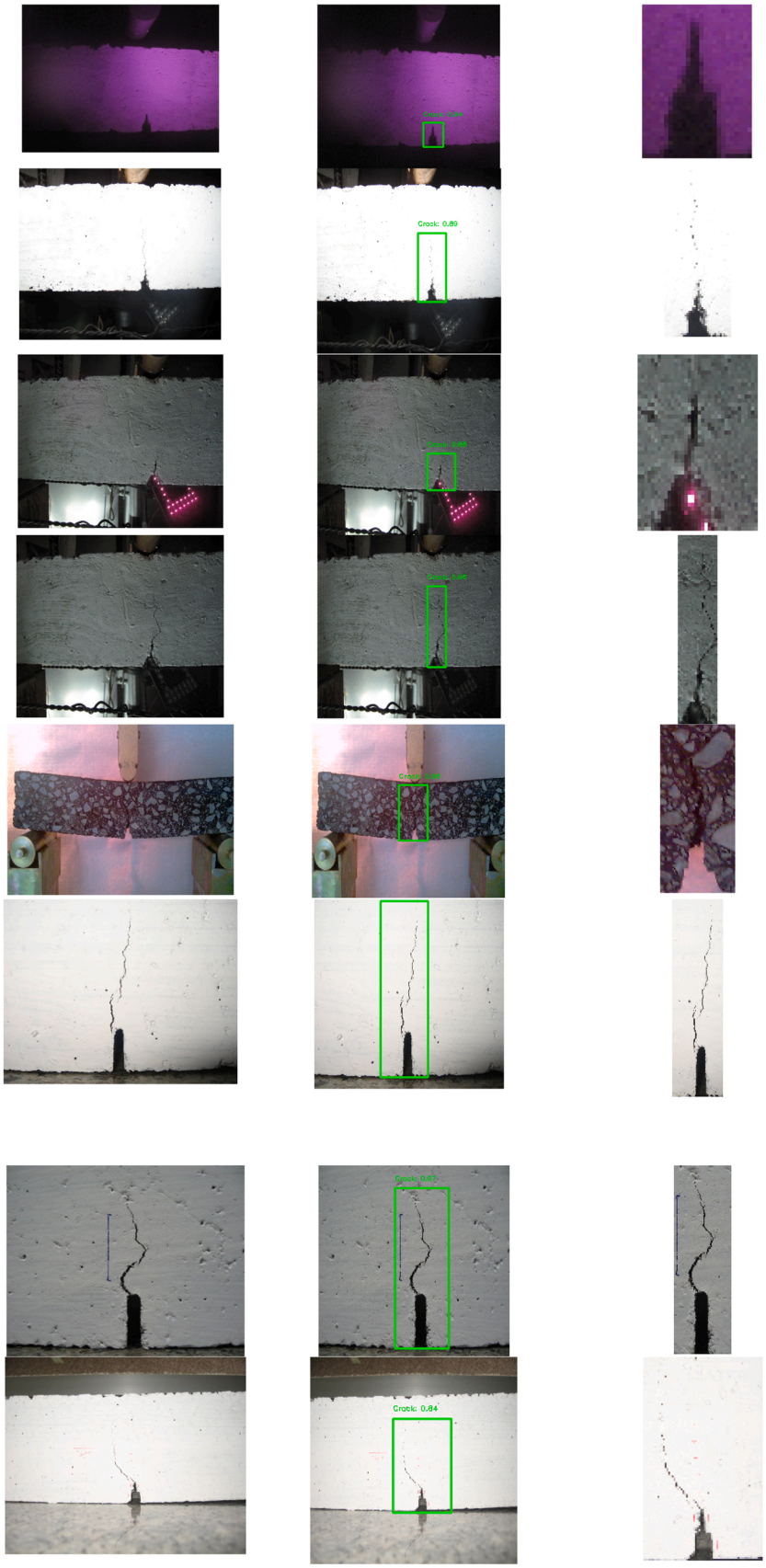

Fig. 8. Sample CNN crack detections.

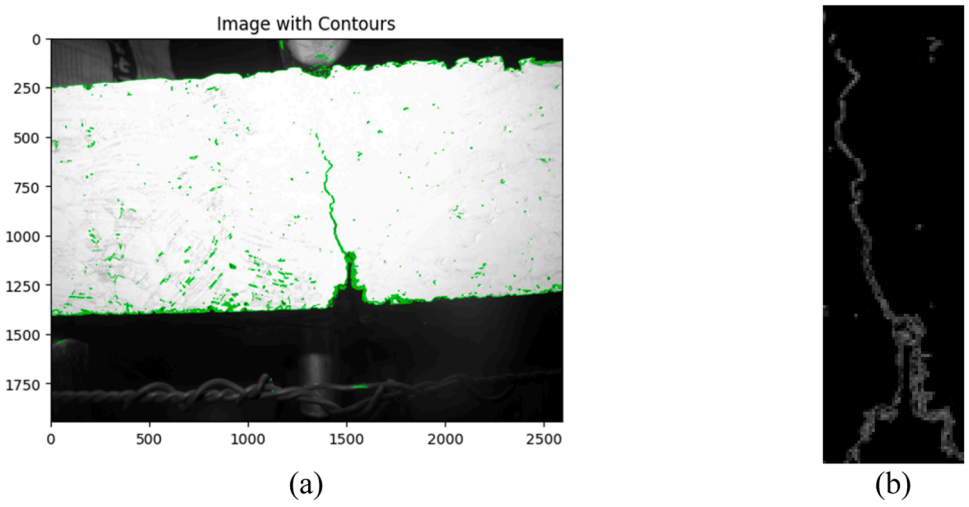

Fig. 9. Sample continuous crack contours for calculation of crack length: a) Edge detection on the AC beam, and b) Crack contours over the threshold cropped image of the crack.

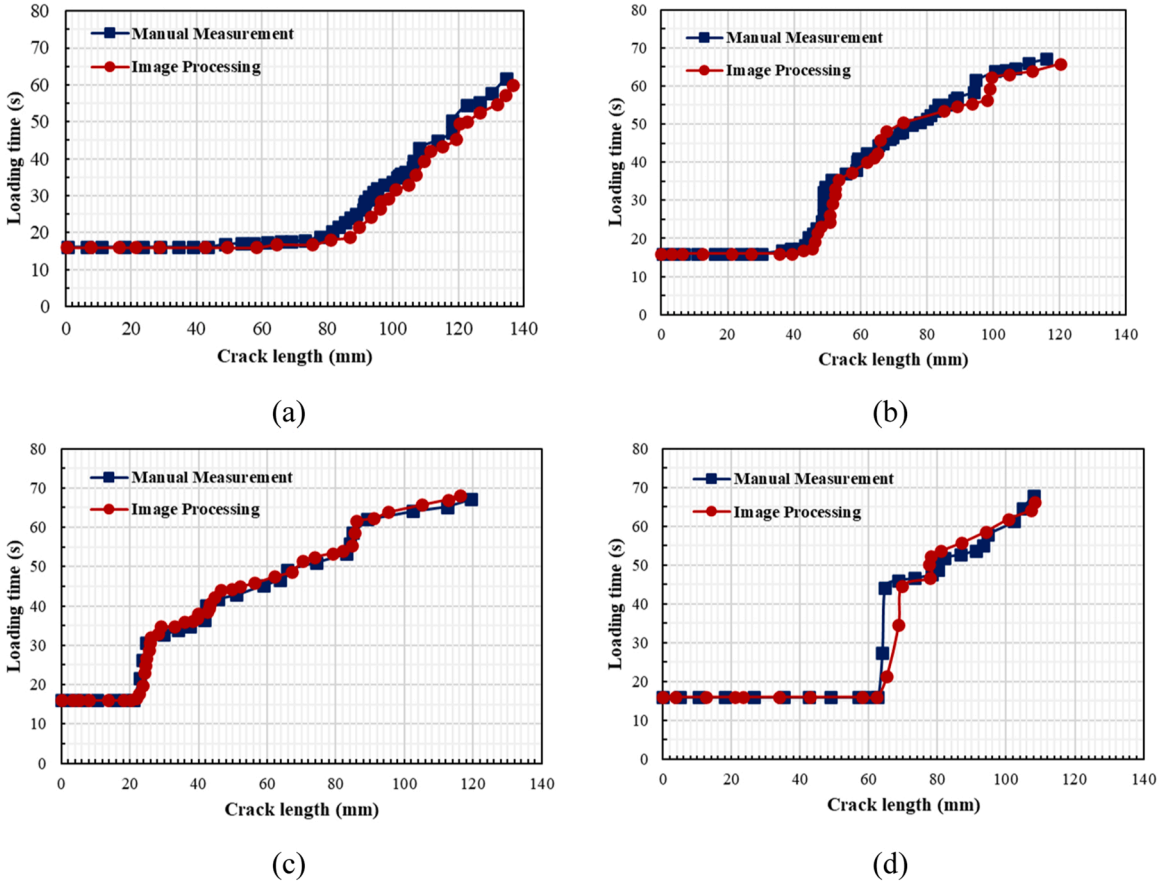

Fig. 10. Crack extensions during the test: a) T=0 °C, PG58–22, Limestone aggregate, b) T=-15 °C, PG58–22, Limestone aggregate, c) T=0 °C, PG58–22, Siliceous aggregate, d) T=-15 °C, PG58–22, Siliceous aggregate.

lower brittleness in lower temperatures, and hence exhibiting higher energy dissipation characteristics. Excluding the transition zone from crack (notch) tip blunting phase to the unstable crack propagation phase for the mixture with siliceous aggregate at T=-15 °C, it can be seen that the automated deep learning-based method has seamlessly determined the R-curve.

Fracture resistance curves at T=-20 °C are presented separately in Fig. 13 (a) to (d) to scrutinize the performance of the automated framework at lower temperatures. Limestone mixtures exhibit higher R-curves than siliceous mixtures. However, all the mixtures undergo a plateaued resistance curve in the unstable propagation zone which means that the crack propagation is highly unstable bringing the mixture (and the AC layer in the pavement structure) to an abrupt fracture failure. The transition zone between the crack blunting phase and the unstable propagation is substantially small in this test temperature due to the embrittlement of the binder. As can be seen in Fig. 13 (a)

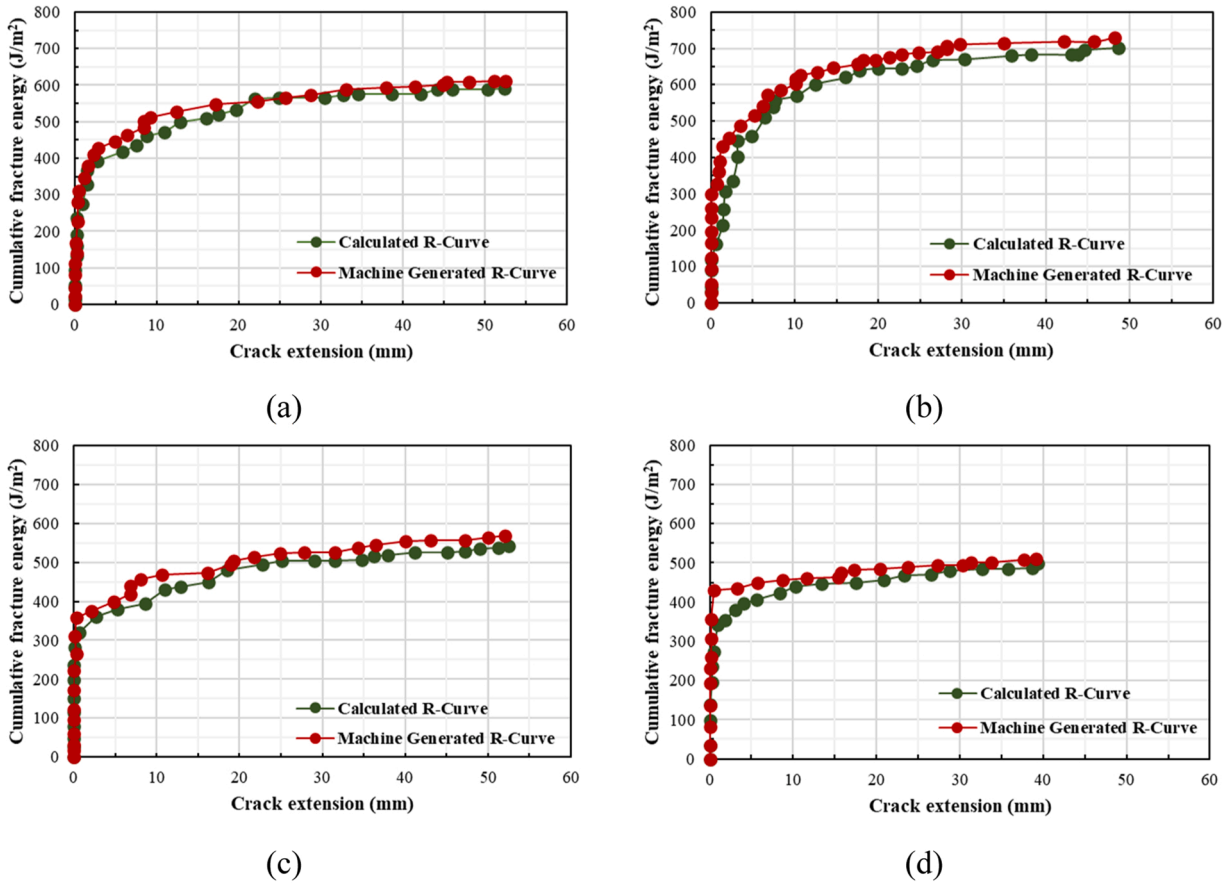

Fig. 11. R-curves for mixtures with PG58–22 binder: a) Limestone aggregate at 0 °C, b) Limestone aggregate at −15 °C, c) Siliceous aggregate at 0 °C, d) Siliceous aggregate at −15 °C.

to (d), the R-curve obtained from the automated framework deviates notably in the transition zone from the manually constructed R-curve. This is mainly due to high noise in the captured images at this temperature as well as the rapid transition to the unstable crack propagation phase. Due to the abrupt crack initiation, high-noise (including speckle and temporal [50,51]) images are usually captured in this phase. For crack lengths greater than 0.25 mm, the CNN model is capable of classifying the image as containing a crack while the model drops the image if the initial length is lower. Even though, the CNN model detects the crack in a majority of the images (at least one image acquired with a crack length greater than 0.25 mm for each test), in some cases, the crack extension length could not be measured due to excessive non-Gaussian noise intensity in the captures image. Hence, the R-curve is affected as showing higher magnitudes of cohesive energy in this stage of the fracture process.

Fig. 14 shows fracture resistance curves for the rubberized mixtures at T=-20 °C. Comparing the fracture resistance curves at this temperature, it can be deduced that the incorporation of crumb rubber has contributed to rising the R-curve in the crack blunting phase, and hence the cohesive energy is greater. Additionally, while a notable transition zone is formed again in the curves, the unstable crack propagation zone is also rising and not flat. As this reshaping of the R-curve is attributed to the enhanced temperature insensitivity of the rubberized mixtures, the automated framework has been able to construct the resistance curves more precisely. In the transition zone from crack blunting to stable crack growth, as well as the unstable crack propagation, lower temperature sensitivity of the rubber particles causes further energy dissipations in advancing the crack tip or forming cohesive surfaces. It can be concluded that for mixtures modified with crumb rubber, incorporating crumb rubber enhances the resistance of the mixtures to temperature reduction, resulting in a significant and distinct transition zone within the R-curves. Additionally, within the zone where crack propagation is unstable, the R-curve continues to ascend, instead of remaining flat (compared to the control mixtures as shown in Fig. 13), signifying that energy is being dissipated in this area to further advance the crack tip (indicating resistance). Consequently, a higher number of low-noise images could be acquired during this phase, as the crack develops gradually, allowing the automated system to process them more effectively. Thus, the R-curves of crumb rubber modified mixtures are closely aligned.

This will allow the CNN model to detect more reliably the images containing cracks, with higher number of captured low-noise images input for crack extension measurement.

Three crack propagation parameters: cohesive energy, fracture energy, and energy rate are extracted from the R-curves to quantitatively assess the performance of the automated framework versus the manual method. Fig. 15 (a) presents the magnitudes of the cohesive energy in an equality chart plot. The x-axis represents the values obtained from a manually constructed R-curve while the y-axis corresponds to the automated framework outputs. As previously discussed, inconsistencies in initial crack extension detections may occur due to substantial noise and unstable propagation at the lowest test temperatures where either the CNN model may drop the image containing small low-quality images or the extension could not be measured due to excessive non-Gaussian noise. A notable scatter can be observed in this figure for the cohesive energy magnitudes of 450 J/m^2 to 550 J/m^2 which correspond to specimens tested at −20 °C. However, the Pearson correlation coefficient of r=0.8144 (above 0.5) shows that the automated framework is giving favorably meaningful values, and the trend complies entirely with the manually measured values. Fracture energy magnitude of the

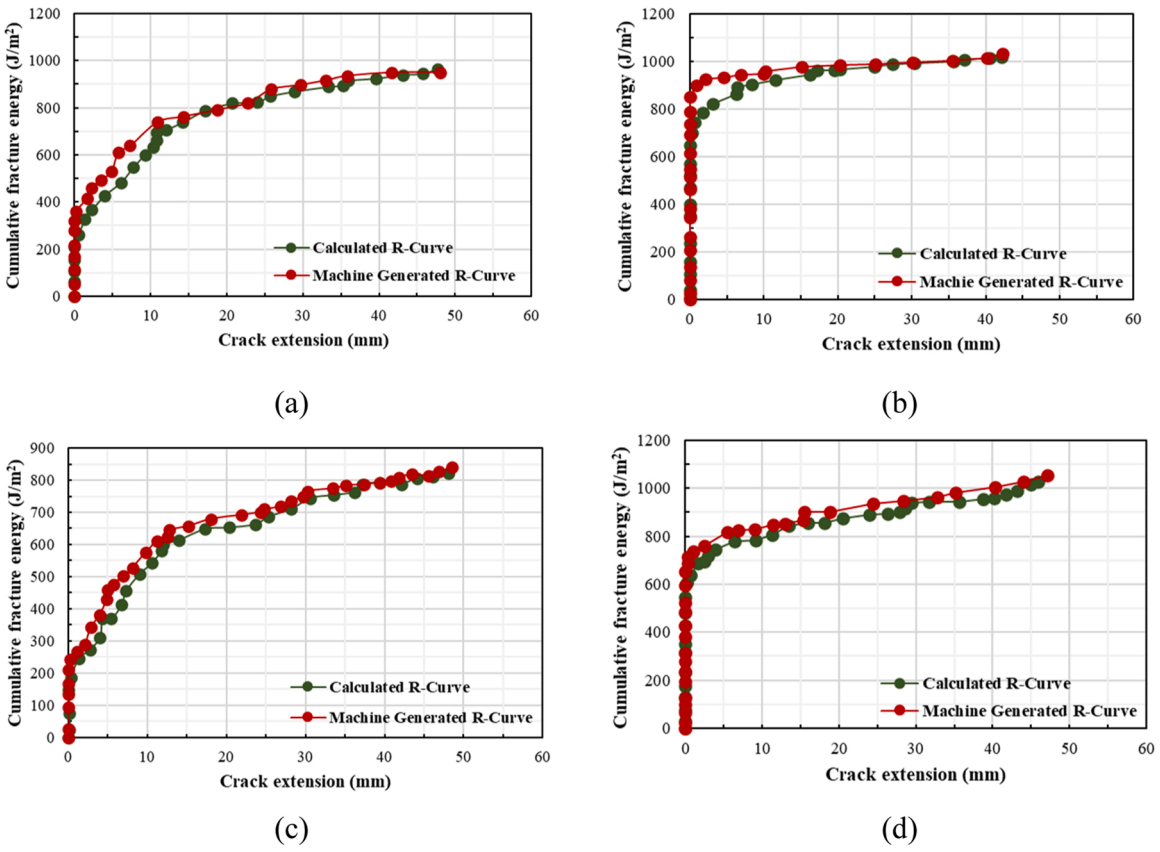

Fig. 12. R-curves for mixtures with PG58–28 binder: a) Limestone aggregate at 0 °C, b) Limestone aggregate at −15 °C, c) Siliceous aggregate at 0 °C, d) Siliceous aggregate at −15 °C.

mixtures, as the most widely used parameter for low-temperature cracking characterization of bituminous mixtures [52–54] is compared in Fig. 15. Fig. 15 (b) shows a substantially condensed plot of fracture energy magnitudes around the equality line. This along with the Pearson correlation coefficient of r=0.98641 shows very close determination of fracture energy magnitudes by the automated framework to those manually obtained. Therefore, the proposed framework could robustly be utilized for fracture energy determination of the mixtures under a broad range of temperatures. Furthermore, a desirable agreement between energy rate magnitudes can be seen from Fig. 15 (c) unless slight scatter around high magnitudes. The energy rate, indicating energy dissipation rates in the unstable crack propagation phase, encompasses a large zone in the R-curve in the post-peak region. Therefore, it can be concluded that the CNN model is capable of detecting images with growing cracks seamlessly and the low-noise images can then be processed with desirable precision. This can further be confirmed from Fig. 11 to Fig. 14 where the unstable crack propagation zones of the R-curves are in significant proximity.

5. Conclusions

In this research, an AI-driven automated framework was developed using convolutional neural networks to generate fracture resistance curves of asphalt concrete mixtures. The CNN model was trained over a dataset of about 1260 images acquired from SE(B) testing of asphalt concrete mixtures with varying temperatures, mixture properties, notch patterns and surface characteristics. Selected images of the AC beam with detected propagating crack were processed and the crack extensions were obtained for the tests establishing the R-curves of each mixture. The following conclusions can be drawn:

- The CNN model consisting of several convolutional layers with increasing filters has exhibited a reliable performance in classifying the images containing the propagating crack and specifying the cracked region in the image. The training accuracy of the model reached beyond 0.84 and the loss remained below 0.15 for the last 30 epochs. A high validation accuracy of 0.97 in the last 30 epochs indicates a desirable performance of the model in classifying SE(B) test images.
- Gaussian blur application and processing of CNN-classified images has shown high accuracy of the crack length measurements. A comparison of crack extensions conducted using this method indicated approximately analogous values of crack growth versus test time while small differences exist due to excessive non-Gaussian noise in captured images in the unstable crack propagation phase.
- For control AC mixtures, as the test temperature is dropped to −20 °C, due to high embrittlement of the binder and mixture, and the greater tendency of the mixtures for unstable crack propagation, initial crack detection by the framework differs slightly from the manually measured values. Therefore, the crack blunting zones in the R-curves resulted from the automated framework are higher in this zone which translates into greater cohesive energy magnitudes.
- As the temperature is reduced in the specimens with siliceous aggregates, the height of the R-curves are reduced significantly in comparison with the limestone mixtures while the curves plateau in the post-peak phase indicating high unstable crack propagation tendency. This effect is more pronounced at −15 °C and −20 °C due to lower bond strength between siliceous aggregates and the binders. For these mixtures, even though a degree of discrepancy is observed for the cohesive energy values determined by the framework and the manually calculated one, however, fracture energy and energy rate

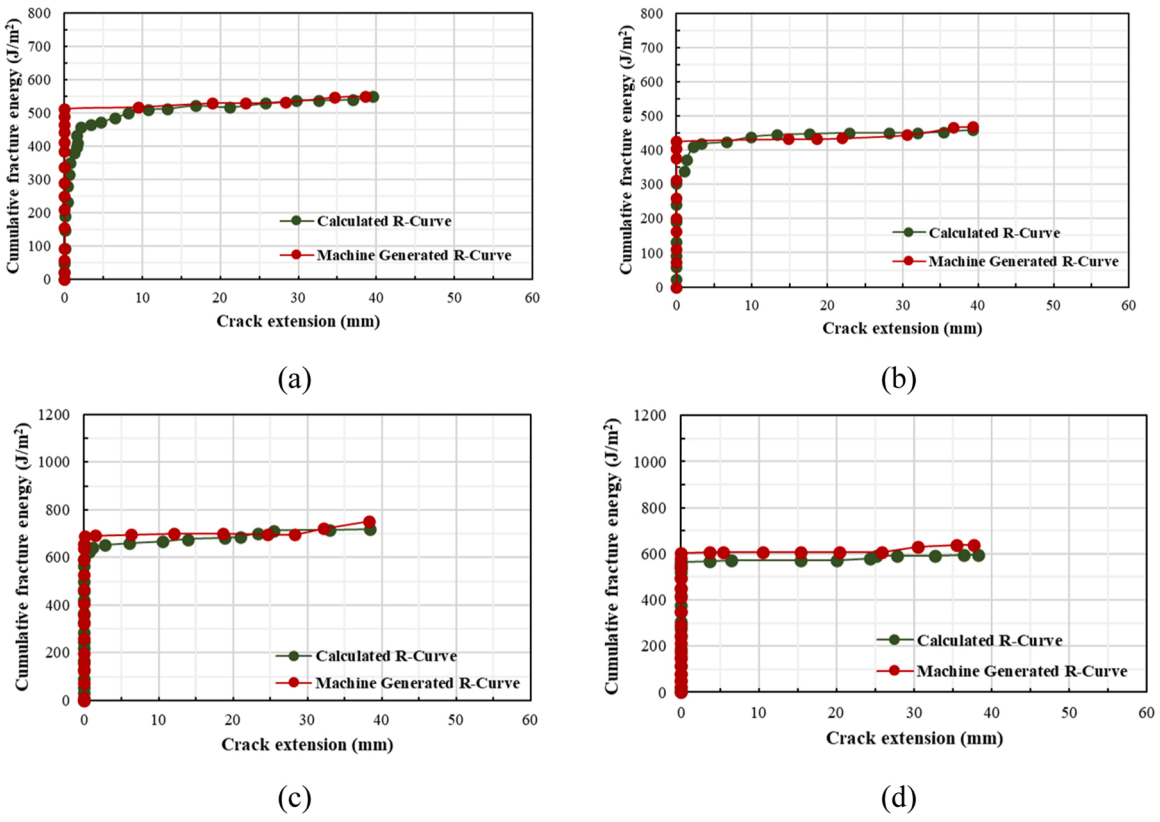

Fig. 13. R-curves for mixtures tested at −20 °C: a) Limestone aggregate with PG58–22 binder, b) Siliceous aggregate with PG58–22 binder, c) Limestone aggregate with PG58–28 binder, d) Siliceous aggregate with PG58–28 binder.

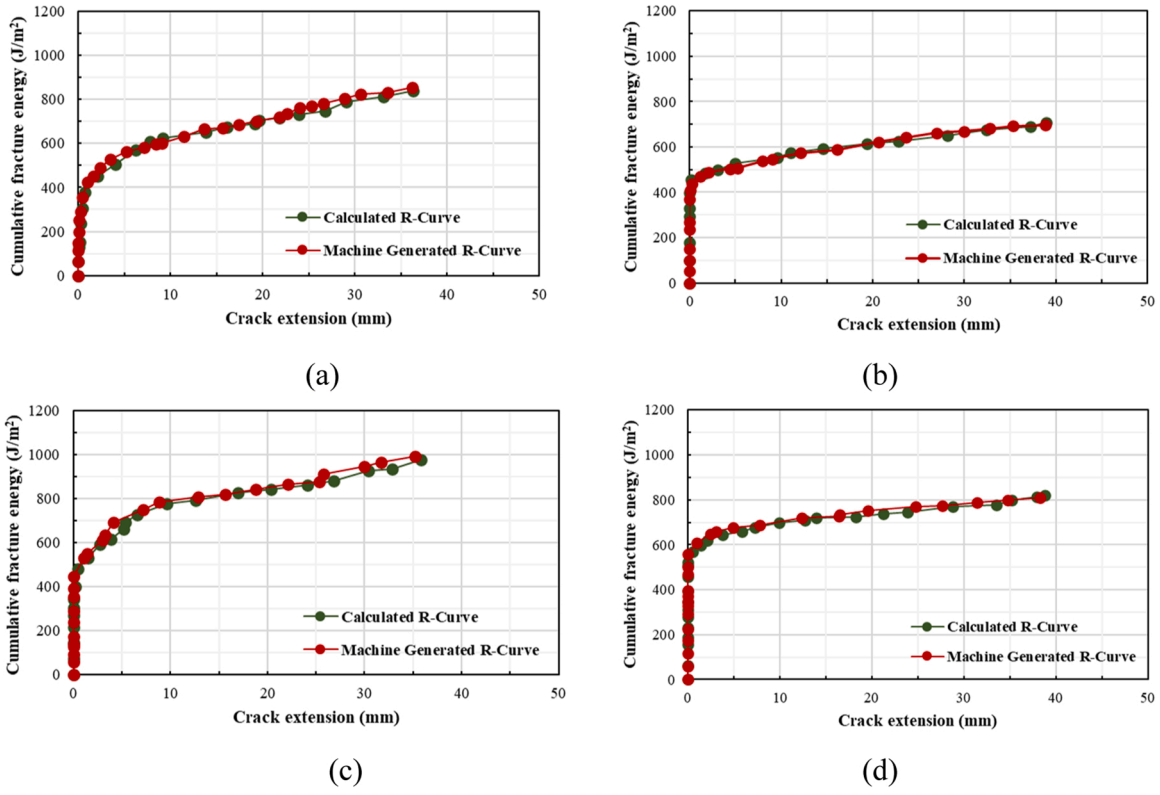

Fig. 14. R-curves for rubberized (20% CR) mixtures tested at −20 °C: a) Limestone with PG58–22 binder, b) Siliceous aggregate with PG58–22 binder, c) Limestone aggregate with PG58–28 binder, d) Siliceous aggregate with PG58–28 binder.

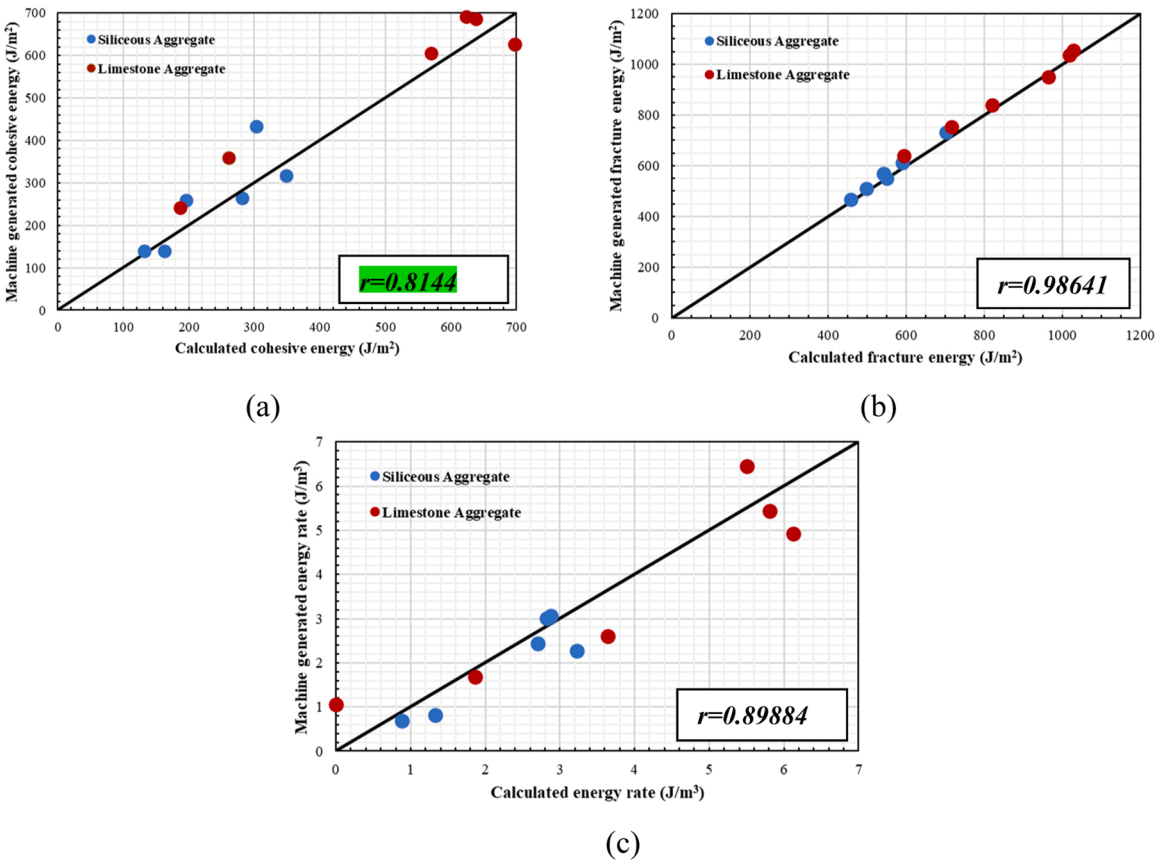

Fig. 15. Comparison of quantitative parameters extracted from R-curves: a) Cohesive energy, b) Fracture energy, c) Energy rate.

values obtained from the automated framework are in very close agreement with the calculated ones.

- As the mixtures are rubberized, further temperature insensitivity is induced in the mixture due to the introduction of crumb rubber particles in the binder. Therefore, notable magnitudes of energy dissipation would be required for an initial crack to extend even at the lowest test temperatures i.e. −20 °C. Moreover, the unstable propagation phase is also energy dissipating which will result in seamless determination of fracture resistance curves by the automated framework.

Depending on the temperature level and mixture properties, test specimens could potentially undergo quasi-brittle to brittle fracture. In this state, crack propagation is abrupt and significantly unstable which results in notable numbers of high-noise images complicating automated classification and extension calculations. AI-driven noise reduction and image enhancement techniques with crack propagation pattern predictions can be developed and embedded into he framework to enhance such images prior to the binary classification stage.

Funding Body

There is no Funding support for this research.

Ethical Statement

The paper has been submitted with full responsibility, following due ethical procedure, and there is no duplicate publication, fraud, plagiarism. None of the authors of this paper has a financial or personal relationship with other people or organizations that could inappropriately influence or bias the content of the paper.

CRediT authorship contribution statement

Hadi Kazemi: Writing – review & editing, Visualization, Validation. **Sepehr Ghafari:** Writing – original draft, Supervision, Software, Methodology, Investigation, Formal analysis, Data curation, Conceptualization. **Fereidoon Moghadas Nejad:** Writing – review & editing, Supervision, Project administration. **Akbar Sheikh-Akbari:** Writing – review & editing, Visualization, Validation, Methodology, Investigation.

Declaration of Competing Interest

No Competing interests are at stake and there is no conflict of interest with other people or organizations that could inappropriately influence or bias the content of the paper.

Data availability

Data will be made available on request.

References

[1] T.L. Anderson, Fracture Mechanics: Fundamentals and Applications, CRC Press, 2017.
[2] A. Saxena, Advanced Fracture Mechanics and Structural Integrity, CRC Press, 2019.
[3] ASTM-STP 527. Fracture toughness evaluation by R-curve method. Philadelphia, PA, USA: American Society for Testing and Materials; 1973..
[4] X.K. Zhu, J.A. Joyce, J-Resistance curve testing of HY80 steel using SE(B) specimens and normalization method, Eng. Fract. Mech. 74 (2007) 2263–2281.
[5] S. Ghafari, F.M. Nejad, R-Curve behavior and crack propagation properties of asphalt concrete at low temperatures, J. Civ. Eng. Manag. 21 (5) (2015) 559–570, https://doi.org/10.3846/13923730.2014.890653.
[6] S. Ghafari, F.M. Nejad, E. Aflaki, Low temperature J-resistance curve determination of asphalt concrete using wavelet-radon transform, J. Cent. South Univ. 20 (2013) 2563–2569, https://doi.org/10.1007/s11771-013-1769-3.

[7] S. Ghafari, F. Moghadas Nejad, Crack propagation characterization of crumb rubber modified asphalt concrete using J-R curves, Theor. Appl. Fract. Mech. vol. 117 (2022) 103156, https://doi.org/10.1016/j.tafmec.2021.103156.

[8] S. Ghafari, F. Moghadas Nejad, R-Curve Characterization of Crumb Rubber Modified Asphalt Mixtures Incorporating Warm Mix Additive at Low Temperatures, in: Key Engineering Materials, vol. 894, Trans Tech Publ, 2021, pp. 109–114, https://doi.org/10.4028/www.scientific.net/KEM.894.109.

[9] S. Ghafari, F.Moghadas Nejad, H. Kazemi, Low-Temperature Fracture Performance of Polymerized Sulfur Modified Asphalt Concrete Mixtures. Key Engineering Materials, Trans Tech Publ, 2023, pp. 155–160, vol. 951, 10.4028/p-XnEVz3.

[10] S. Yang, A. Braham, Influence of binder grade, gradation, temperature and loading rate on R-curve of asphalt concrete, J, Constr. Build. Mater. 154 (2017) 780–790, https://doi.org/10.1016/j.conbuildmat.2017.08.019.

[11] S. Yang, A. Braham, R-curves characterisation analysis for asphalt concrete, Int. J. Pavement Eng. vol. 19 (2) (2018) 99–108.

[12] S. Ghafari, F. Moghadas Nejad, Effect of mode mixity, temperature, binder content, and gradation on mixed mode (I/II) R-curve of asphalt concrete at low temperatures, /12/27/ 2021, Constr. Build. Mater. vol. 313 (2021) 125567, https://doi.org/10.1016/j.conbuildmat.2021.125567.

[13] S. Ghafari, F.Moghadas Nejad, Developing Mixed-Mode (I/II) Fracture Resistance Curves for Asphalt Concrete Mixtures at Low Temperatures, in: Key Engineering Materials, vol. 958, Trans Tech Publ, 2023, pp. 195–199, https://doi.org/10.4028/p-bSXzr2.

[14] S. Ghafari, F.Moghadas Nejad, H. Kazemi, Developing a Single-Specimen Technique for Low-Temperature R-Curve Determination of Asphalt Concrete Using a Modified Unloading Compliance Method, in: Key Engineering Materials, vol. 951, Trans Tech Publ, 2023, pp. 141–146, https://doi.org/10.4028/p-Z0h762.

[15] T. Liu, S. Yang, A. Braham, R. Huang, An alternative of crack extension in R-curve analysis of asphalt concrete, J, Constr. Build. Mater. 265 (2020) 120741, https://doi.org/10.1016/j.conbuildmat.2020.120741.

[16] Anqi Chen, Yongli Zhao, Pengbo Li, Yuanyuan Li, Monketh Mohammed, Peng Guo, Crack propagation prediction of asphalt pavement after maintenance as a function of initial cracks distribution, Construction and Building Materials, Volume 231, 2020,117157, ISSN 0950-0618, https://doi.org/10.1016/j.conbuildmat.2019.117157.

[17] Ganghua Hu, Qing Yang, Xin Qiu, Dingchuan Zhang, Wenhao Zhang, Shanglin Xiao, Jingxian Xu, Use of DIC and AE for investigating fracture behaviors of cold recycled asphalt emulsion mixtures with 100% RAP, Construction and Building Materials,Volume 344,2022,128278,ISSN 0950-0618, https://doi.org/10.1016/j.conbuildmat.2022.128278.

[18] Zhaohui Pei, Peng Xiao, Keke Lou, Xing Wu, Influence of fiber-asphalt interface property on crack resistance of asphalt mixture, ISSN 2214-5095, Case Stud. Constr. Mater. Volume 17 (2022) e01703, https://doi.org/10.1016/j.cscm.2022.e01703.

[19] N. Hasheminejad, C. Vuye, A. Margaritis, B. Ribbens, G. Jacobs, J. Blom, W. Van den bergh, J. Dirckx, S. Vanlanduit, Investigation of Crack Propagation and Healing of Asphalt Concrete Using Digital Image Correlation, Appl. Sci. 9 (12) (2019) 2459, https://doi.org/10.3390/app9122459.

[20] M.F. Asghar, M.J. Khattak, Evaluation of Mixture Design and Tensile Characteristics of Polyvinyl Alcohol (PVA)-Fiber Reinforced HMA Mixtures, Int. J. Pavement Res. Technol. (2022).

[21] M.F. Asghar, M.J. Khattak, K.S. Fericy, M. Manfra, Development of high performing hybrid hot mix asphalt mixtures, Int. J. Pavement Eng. 24 (1) (2023) 2241962.

[22] M.F. Asghar, M.J. Khattak, Fracture and fatigue characteristics of high performing novel hot mix asphalt composites, Constr. Build. Mater. 383 (2023) 131217.

[23] S. Ghafari, M. Ehsani, F.M. Nejad, Prediction of low-temperature fracture resistance curves of unmodified and crumb rubber modified hot mix asphalt mixtures using a machine learning approach, Constr. Build. Mater. vol. 314 (2022) 125332, https://doi.org/10.1016/j.conbuildmat.2021.125332.

[24] X. Li, A. Braham, M. Marasteanu, W. Buttlar, Effect of Factors Affecting Fracture Energy of Asphalt Concrete at Low Temperature, Road. Mater. Pavement Des. 9 (2008) 397–416.

[25] M. Ahmad, B.K. Bairgi, Z.H. Khan, et al., Evaluation of the fracture resistance of asphalt concrete mixes including the effect of anisotropy, Int. J. Pavement Res. Technol. 13 (2020) 121–128, https://doi.org/10.1007/s42947-019-0092-2.

[26] S. Ghafari, S. Ranjbar, M. Ehsani, Sustainable crumb rubber modified asphalt mixtures based on low-temperature crack propagation characteristics using the response surface methodology, Theor. Appl. Fract. Mech. vol. 123 (2023) 103718, https://doi.org/10.1016/j.tafmec.2022.103718.

[27] S. Pirmohammad, M. Khanpour, Fracture strength of warm mix asphalt concretes modified with crumb rubber subjected to variable temperatures, Road. Mater. Pavement Des. 21 (2020) S57–S75, https://doi.org/10.1080/14680629.2020.1724819.

[28] B. Crisman, G. Ossich, et al., A Laboratory Assessment of the Influence of Crumb Rubber in Hot Mix Asphalt with Recycled Steel Slag, Sustainability 12 (2020) 8045, https://doi.org/10.3390/su12198045.

[29] L. Xiang, J. Cheng, G. Que, Microstructure and performance of crumb rubber modified asphalt, Constr. Build. Mater. 23 (2009) 3586–3590, https://doi.org/10.1016/j.conbuildmat.2009.06.038.

[30] H. Wang, X. Liu, M. van de Ven, G. Lu, S. Erkens, A. Skarpas, Fatigue performance of long-term aged crumb rubber modified bitumen containing warm-mix additives, J, Constr. Build. Mater. 239 (2020) 117824, https://doi.org/10.1016/j.conbuildmat.2019.117824.

[31] M.P. Wagoner, W.G. Buttlar, G.H. Paulino, Development of a single-edge notched beam test for the study of asphalt concrete fracture, Adv. Pavement Eng. (2005) 1–13.

[32] M.P. Wagoner, W.G. Buttlar, G.H. Paulino, Development of a single-edge notched beam test for asphalt concrete mixtures, J. Test. Eval. vol. 33 (6) (2005) 452–460.

[33] Standard Test Method for Linear-Elastic Plane-Strain Fracture Toughness of Metallic Materials, ASTM E399-20a, ASTM International, West Conshohocken, PA, 2020. ⟨www.astm.org⟩.

[34] ASTM E1820–20b, Standard Test Method for Measurement of Fracture Toughness, ASTM International, West Conshohocken, PA, 2020, www.astm.org..

[35] S. Pirmohammad, M.R. Ayatollahi, Asphalt concrete resistance against fracture at low temperatures under different modes of loading, Cold Reg. Sci. Technol. 110 (2015) 149–159.

[36] M. Fakhri, E. Haghighat Kharrazi, M.R.M. Aliha, Mixed mode tensile-in plane shear fracture energy determination for hot mix asphalt mixtures under intermediate temperature conditions, Eng. Fract. Mech. 192 (2018) 98–113, https://doi.org/10.1016/j.engfracmech.2018.02.007.

[37] M.R. Eghbali, M.F. Tafti, M.R.M. Aliha, H. Motamedi, The effect of ENDB specimen geometry on mode I fracture toughness and fracture energy of HMA and SMA mixtures at low temperatures, Eng. Fract. Mech. 216 (2019) 106496, https://doi.org/10.1016/j.engfracmech.2019.106496.

[38] M.R.M. Aliha, S. Shaker, Effect of bitumen type, temperature, and aging on mixed I/II fracture toughness of asphalt binders- Experimental and theoretical assessment, Theor. Appl. Fract. Mec. 110 (2020) 102801, https://doi.org/10.1016/j.tafmec.2020.102801.

[39] H. Motamedi, H. Fazaeli, M.R.M. Aliha, Evaluation of temperature and loading rate effect on fracture toughness of fiber reinforced asphalt mixture using edge notched disc bend (ENDB) specimen, J, Constr. Build. Mater. 234 (2020) 117365, https://doi.org/10.1016/j.conbuildmat.2019.117365.

[40] T.C. RILEM, "FMC 1 Determination of the fracture energy of mortar and concrete by means of three-point bend tests on notched beams, 1985,", RILEM Recomm. Test. Use Constr. Mater. (1994) 99–101.

[41] C. Bishop, Neural Networks for Pattern Recognition, Oxford University Press, 1995.

[42] M. Augusteijn, T. Harrington, Evolving transfer functions for artificial neural Networks, Neural Comput. Appl. 13 (2004) 38–46, https://doi.org/10.1007/s00521-003-0393-9.

[43] N. Srivastava, G. Hinton, A. Krizhevsky, I. Sutskever, R. Salakhutdinov, Dropout: A simple way to prevent neural networks from overfitting, J. Mach. Learn. Res. 15 (2014) 1929–1958.

[44] I. Goodfellow, Y. Bengio, A. Courville, Deep learning, volume 1, MIT press, Cambridge, 2016.

[45] T. Tieleman, G. Hinton, Lecture 6.5-rmsprop: Divide the Gradient by a Running Average of Its Recent Magnitude, COURSERA: Neural Netw. Mach. Learn. 4 (2012) (2012) 26–31.

[46] D.P. Kingma, J.L. Ba, Adam: A Method for Stochastic Optimization, 3rd Int. Conf. Learn. Represent. (2015), https://doi.org/10.48550/arXiv.1412.6980.

[47] M. Sokolova, N. Japkowicz, S. Szpakowicz, Beyond Accuracy, F-Score and ROC: A Family of Discriminant Measures for Performance Evaluation. In: Sattar, A., Kang, Bh. (eds) AI 2006: Advances in Artificial Intelligence. AI 2006. Lecture Notes in Computer Science(.), vol 4304. Springer, Berlin, Heidelberg. https://doi.org/10.1007/11941439_114.

[48] A. Ruby, P. Theerthagiri, I.J. Jacob, Y. Vamsidhar, Binary cross entropy with deep learning technique for image classification, Int. J. Adv. Trends Comput. Sci. Eng. 9 (2020) 5393–5397.

[49] P. Chun, S. Izumi, T. Yamane, Automatic detection method of cracks from concrete surface imagery using two-step light gradient boosting machine, Comput. -Aided Civ. Infrastruct. Eng. 36 (2021) 61–72, https://doi.org/10.1111/mice.12564.

[50] R. Ren, Z. Guo, Z. Jia, et al., Speckle Noise Removal in Image-based Detection of Refractive Index Changes in Porous Silicon Microarrays, Sci. Rep. 9 (2019) 15001, https://doi.org/10.1038/s41598-019-51435-y.

[51] O. Karaoğlu, H.Ş. Bilge, İ. Uluer, Removal of speckle noises from ultrasound images using five different deep learning networks, Eng. Sci. Technol., Int. J. 29 (2022) 101030, https://doi.org/10.1016/j.jestch.2021.06.010.

[52] AASHTO TP 105, Standard Method of Test for Determining the Fracture Energy of Asphalt Mixtures Using the Semicircular Bend Geometry (SCB), 2020..

[53] AASHTO T 394, Standard Method of Test for Determining the Fracture Energy of Asphalt Mixtures Using the Semicircular Bend Geometry (SCB), 2022..

[54] ASTM D7313–20, Standard Test Method for Determining Fracture Energy of Asphalt Mixtures Using the Disk-Shaped Compact Tension Geometry, ASTM International, West Conshohocken, PA, 2020, www.astm.org..